Journal of Alloys and Compounds 725 (2017) 1188–1198

Contents lists available at ScienceDirect

Journal of Alloys and Compounds

journal homepage: http://www.elsevier.com/locate/jalcom

Multilayer design of CrN/MoN protective coatings for enhanced hardness and toughness

B.O. Postolnyi [a, b, *], V.M. Beresnev [c], G. Abadias [d], O.V. Bondar [a], L. Rebouta [e], J.P. Araujo [b], A.D. Pogrebnjak [a, *]

[a] Sumy State University, 2 Rymskogo-Korsakova St., 40007, Sumy, Ukraine
[b] IFIMUP and IN - Institute of Nanoscience and Nanotechnology, Department of Physics and Astronomy, Faculty of Sciences, University of Porto, 687 Campo Alegre St., 4169-007, Porto, Portugal
[c] V.N. Karazin Kharkiv National University, 4 Svobody Sq., 61022, Kharkiv, Ukraine
[d] Institut Pprime, Department of Physics and Mechanics of Materials, CNRS – University of Poitiers – ENSMA, 11 Blvd. M. et P. Curie, BP 30179, F-86962, Chasseneuil-Futuroscope Cedex, France
[e] Centre of Physics, University of Minho, Azurém, 4800-058, Guimarães, Portugal

ARTICLE INFO

Article history:
Received 12 May 2017
Received in revised form
29 June 2017
Accepted 2 July 2017
Available online 3 July 2017

Keywords:
Nitrides
Hard coatings
Physical vapour deposition
Diffraction
Structure
Mechanical properties

ABSTRACT

We report on CrN/MoN multilayer coatings, their structure, elemental and phase composition, residual stresses, mechanical properties and their dependence on deposition conditions. The hardness and toughness were considered as main parameters for improvement of the protective properties of coatings. Multilayers with varying bilayer periods, ranging from 40 nm to 2.2 μm, were obtained by using cathodic arc physical vapour deposition (Arc-PVD) on stainless steel substrate. The elemental analysis was performed using wavelength-dispersive X-ray spectroscopy (WDS). The surface morphology and cross-sections were analysed with scanning electron microscopy (SEM). The X-ray diffraction (XRD) measurements, including grazing incidence X-ray diffraction (GIXRD), in-plane diffraction analysis and electron backscatter diffraction (EBSD), were used for microstructure characterisation. Mechanical properties of deposited films were studied by measuring hardness (H) and Young's modulus (E) with micro-indentation, H/E and H^3/E^2 ratios were calculated. The dependences of internal structure and, hence, mechanical properties, on layer thickness of films have been found. Significant enhancement of hardness and toughness was observed with decreasing individual layer thickness to 20 nm: H = 38–42 GPa, H/E = 0.11.

1. Introduction

It is well known that various surface modification techniques (ion implantation, surface oxidation, ablation, protective coatings, etc.) [1–4] are widely used nowadays to satisfy the needs of engineering, industry and business, in materials with desirable properties for an acceptable price. Hard coatings are the most efficient in providing protection from deformation and wear [5–12]. But often hard materials may be brittle and prone to cracking, which is why for protective coatings, it is crucial to have both high hardness and toughness. Transition metal nitrides (TMN) are largely employed as hard protective coatings in the cutting and forming tool industry, as they exhibit high hardness, chemical inertness and thermal stability under harsh environments (oxidation, radiation). Research strategies are currently deployed to improve their toughness, by synthesizing multicomponent systems [13–15] and/or tailoring their architecture through interface control (e.g., in superlattices) [16–18].

TiN has been the most widely studied TMN protective coating and it's still widely used since the late 1960s [19–21]. However, it has some limitations and hardly overcomes modern challenges. The weak point of such coatings is the thermal stability and oxidation resistance. Under high temperature, an oxide layer may be formed on the surface, which develops stress in the coating, high enough to damage or destroy the protective layers. For TiN it happens at a temperature above 500 °C [22,23]. CrN also has similar properties, but has higher thermal stability (more than 600 °C [24–26]), extremely strong adhesion to metal substrate, higher

* Corresponding authors.
E-mail addresses: b.postolnyi@gmail.com (B.O. Postolnyi), alexp@i.ua (A.D. Pogrebnjak).

http://dx.doi.org/10.1016/j.jallcom.2017.07.010
0925-8388/

corrosion and wear resistance. Compared to all other TMN, though MoN is the hardest superconducting metal nitride, it has been studied much less, despite exhibiting hardness of about 28–34 GPa. Various phases with a wide range of stoichiometry and lattice structure have been reported [27–32]: cubic γ-$Mo_2N_{1\pm x}$, tetragonal β-$Mo_2N_{1\pm x}$, hexagonal δ-MoN and metastable MoN_x phase of NaCl-B1-type cubic structure.

Improvement of mechanical properties and oxidation/wear resistance of TMN may be gained from multilayer design of TMN coatings, which benefit from the synergistic effect of individual layer properties, as well as Hall-Petch strengthening. Combined with TiN, it has been recently shown that TiN/MoN multi-layered coatings showed successful enhancement of mechanical properties [33–38]. The aim of the present paper is to investigate the structure, phase composition and mechanical properties of multilayer CrN/MoN coatings, for which reported work is limited [39–45]. Their dependence on bilayer thickness and grain size will be discussed, in anticipation of further significant improvement.

2. Multilayer deposition

CrN/MoN multi-layered coatings were fabricated by cathodic arc physical vapour deposition (Arc-PVD) on steel substrates, using vacuum-arc unit "Bulat-6M", designed for deposition of protective and decorative coatings (see schematic in Fig. 1). Films were deposited on the polished substrates of stainless steel 12X18H9T with dimensions of 20 × 20 mm^2 and thickness of 2 mm. Before the deposition process, the substrate surface was cleaned and activated by metal ion bombardment, by applying the negative potential of −1.3 kV to the substrates for 15 min. Cleaning process was performed under continuous rotation of substrate holder and arc current I_{arc} of 120 and 100 A for Cr (chromium X99 rod, purity of 99%) and Mo (pure vacuum melted molybdenum rod, purity 99.99%) cathodes respectively. Then the interlayers of pure metals were deposited during 1 min and the main process of multilayer CrN/MoN films deposition was performed in nitrogen atmosphere, up to 1 h. Automatic control system of substrate holder rotation provides static position of substrates, when facing the targets (during alternate layer deposition), and then rotation to other evaporation source while cathodes are switched off until a new position of substrate holder is reached.

The deposition time per layer was varied from 300 to 10 s from sample 1 to sample 6 while other deposition conditions were maintained in similar states (see Table 1). Coatings have between 12 and 354 layers each, and the thickness of single layer varies from tens nanometres up to 1.1 μm, corresponding to total film thickness in the range of 7.8–14.7 μm.

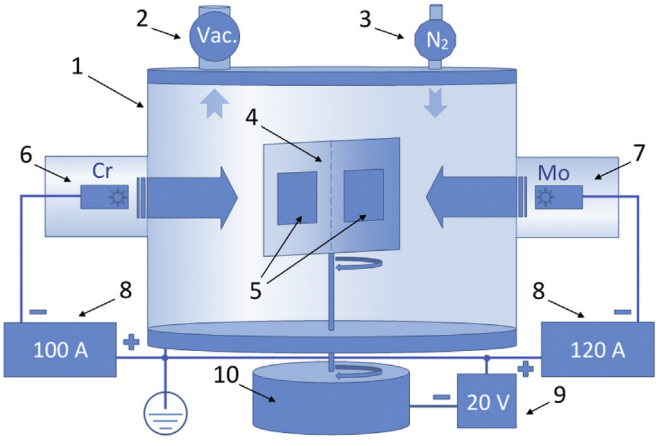

Fig. 1. Vacuum-arc deposition system for multilayer films. 1 – vacuum chamber, 2 – vacuum pump system, 3 – nitrogen supply, 4 – substrate holder, 5 – substrates, 6 – chromium evaporator, 7 – molybdenum evaporator, 8 – arc power supplies, 9 – substrate power supply, 10 – automatic rotation system for substrate holder.

3. Characterisation methods

The surface morphology analysis and films cross-section observations were performed by scanning electron microscopy (SEM), using JEOL JSM-7001F Schottky Emission Scanning Electron Microscope and FEI Quanta 400 FEG Environmental SEM (ESEM). Cross-section samples were prepared by cutting of coatings and substrates with further hot mounting into conductive epoxy resin and, finally, by grinding and polishing.

The elemental analysis was obtained by wavelength-dispersive X-Ray spectroscopy (WDS) using an Oxford Instruments INCA WAVE WDS spectrometer unit attached to the above mentioned JEOL JSM-7001F and by INCAEnegy+ software module. The WDS scanning was performed successively by $K\alpha_1$ lines for Cr, N, O elements and by $L\alpha_1$ line for Mo using 10 kV high accelerating voltage, probe current of 20 nA and magnification in range from ×1,000 to ×5,000. This technique is complementary to the energy-dispersive spectroscopy (EDS), or can run independently. The WDS spectrometers have significantly higher spectral resolution and enhanced quantitative potential.

The calculation of electron beam penetration depth in thin films was done using equation (1) [46]:

$$x = \frac{0.1E_0^{1.5}}{\rho}, \quad (1)$$

where E_0 is the energy of incident electrons in keV; ρ – density of the material in g/cm^3.

The X-ray diffraction (XRD) analysis was performed in Bragg-Brentano geometry (θ/2θ), using Panalytical X'Pert Pro Multipurpose Diffractometer. The XRD patterns were acquired by exposing samples to Cu Kα X-ray radiation, which has a characteristic wavelength $\lambda_{K\alpha1}$ = 1.5405980 Å (mainly) and $\lambda_{K\alpha2}$ = 1.5444260 Å, ratio of intensities $K\alpha_1/K\alpha_2$ = 0.5. They were generated by PW3373/00 (Cu LFF DK292308) X-ray tube operated at U_{acc} = 40 kV and I_{emis} = 30 mA in the line focus mode with 12.0 mm length and 0.4 mm width. The data were collected over the range 2θ = 10÷95° with the step size 2θ = 0.017° and the scan speed 2°/min, using the scanning X'Celerator detector. The fixed divergence slit of 0.5° was used together with the beam mask of 5 mm and all scans were carried out in continuous mode. Incident and receiving soller slits were 0.04 rad, receiving slit was 0.1°.

Complementary (θ/2θ) scan and additional XRD analysis in low-angle range (GIXRD and in-plane diffraction), as well as residual stresses measurements, were performed using high-resolution X-ray diffractometer Rigaku SmartLab. Spectra were acquired by using various optics, scan speed and scan step, applying the parallel beam of Cu Kα X-ray radiation with $\lambda_{K\alpha1}$ = 1.540593 Å and

Table 1
Conditions of Arc-PVD deposition for studied CrN/MoN coatings.

Sample number	I_{arc}, A		U_b, V	p, Pa	Dep. time per layer, s	Number of layers
	MoN	CrN				
1	120	100	−20	0.4	300	12
2					150	25
3					80	45
4					40	88
5					20	180
6					10	354

$\lambda_{K\alpha 2}$ = 1.544414 Å generated by rotating copper anode at U_{ac} = 45 kV and I_{emis} = 200 mA in line focus mode with 8.0 mm length and 0.4 mm width.

It should be noted that in contrast to the normal θ/2θ scanning, where the scattering vector is perpendicular to the surface, in X-ray analysis such as in-plane XRD, the scattering vector lies parallel to the film surface and the diffraction can be observed from the lattice planes normal to the samples surface. In asymmetric GIXRD, the scattering vector is inclined to the film's surface and changes its position continuously with changing of 2θ value. Therefore, depending on the detector position, various planes normal to the current scattering vector in each point of time will contribute to the total diffraction pattern of the sample.

The evaluation of crystallites sizes was carried out using Scherrer equation (2) [47]:

$$d = \frac{K\lambda}{\beta \cos\theta}, \quad (2)$$

where d is a mean size of the ordered (crystalline) domains, which may be smaller or equal to the grain size, in Å; λ is an X-ray wavelength, in Å; β is a line broadening at half the maximum intensity (FWHM) in radians; θ is the Bragg angle, in radians; K ≈ 0.89 is a dimensionless shape factor depending on (hkl) Miller indexes.

The EBSD analysis was performed using the unit of EDAX EBSD forward scatter detector system and high resolution DigiView III camera attached to the above mentioned FEI Quanta 400 FEG ESEM. The grain tolerance angle of 5° was used for grains determination. Grains at edges of scans were not included in statistics.

Calculation of residual stress was performed by $\sin^2\psi$ method, using asymmetric XRD 2θ scans for various fixed incident ω angles and assuming zero values of φ and χ angles [48–50]. The angle ψ was found by subtracting ω from θ. The scheme of the experiment is shown in Fig. 2.

Out-of-plane lattice constants $a_\perp$ were determined from d-spacing vs $\sin^2\psi$ plots, as well as from XRD θ/2θ patterns, while in-plane lattice constants $a_\parallel$ were deduced from in-plane XRD data.

The analysis of mechanical properties was realised by micro-indentation for hardness and Young's modulus (elastic modulus) measurements. The NanoTest instrument from Micro Materials company was used. On each sample, up to 10 indentations oriented in one line with the interval of 50 μm were made. The NanoTest instrument has Berkovich indenter and uses the method of depth sensing indentation with the collected data analysis performed by supplied software using Oliver-Pharr method. The measured data was collected in "Depth Vs Load Hysteresis" mode with an acquisition process controlled by penetration depth. The maximum penetration depth was in the range 0.6–1.3 μm, but not deeper than 10% of coating thickness and the maximum load reached values of 583 mN.

4. Results and discussion

4.1. Multilayer structures

The multilayer structure of studied CrN/MoN coatings achieved by SEM from the polished cross-section samples is presented in Fig. 3. Images of samples 1 and 3 (Fig. 3 (a) and (b)) were taken in secondary electron imaging (SEI) mode, magnification ×5,000 and ×15,000 respectively. Image of sample 6 (Fig. 3(c)) was made using backscattered electron detector (BSED) in Z (atomic number) mode, magnification is ×400,000. Summarised results of bilayer and total thickness of coatings are presented in Table 2.

Since heavier atoms with higher atomic number Z give brighter shades of grey on SEM images, the MoN layers with greater average Z will result in brighter layers. CrN layers, on the other hand, have lower average atomic number, thus corresponding to darker layers. The cross-section SEM images confirm the periodic stacking of the MoN/CrN layers and the presence of relatively sharp interfaces, which approves high quality of Arc-PVD deposited films. Defects due to the substrate surface roughness or droplets in films were easily absorbed and smoothed by multilayer structure.

The evolution of deposition rate, calculated by dividing the value of bilayer thickness by the corresponding deposition time (see Table 2), is shown in Fig. 4. It is seen that for coatings with shorter layer deposition time, the real bilayer thickness starts to be lower than predicted by deposition time control. This can be explained by specific features of the deposition system with automatic controller of substrate holder rotation and evaporators power supplies. The shorter the deposition time per layer, the more often does the substrate holder rotate and evaporators are disabled by the controller. Meanwhile, nitrogen flows to the chamber, the excess reactive gas causes increase of pressure and the poisoning of the cathodes and, hence, the decreasing of the evaporation rates. In turn, it also influences the increase of reactive gas again, even at the beginning of the new layer deposition process.

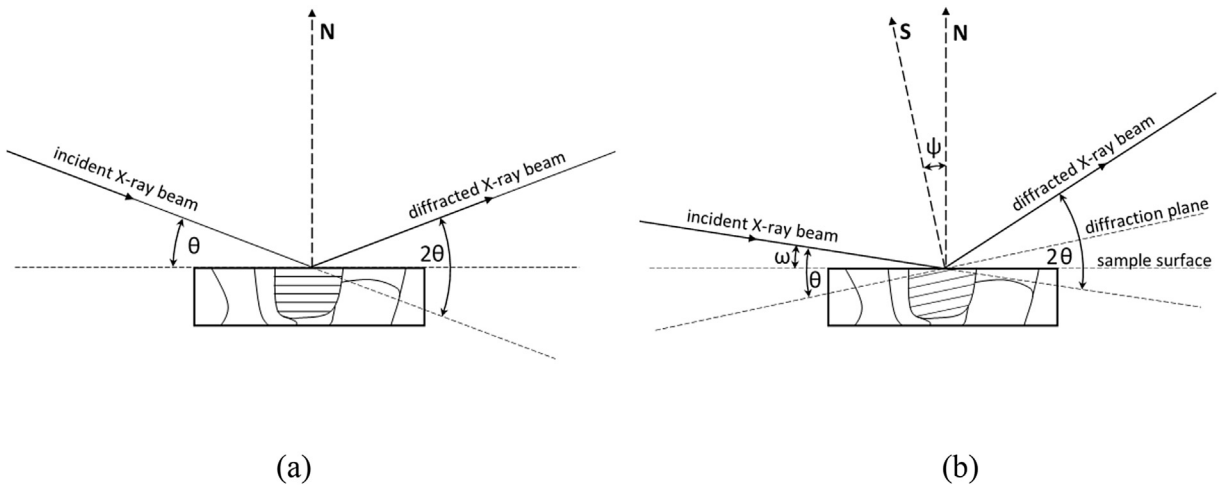

Fig. 2. X-ray diffraction analyses: (a) conventional symmetric θ/2θ scan, (b) asymmetric 2θ scan with fixed position of X-ray source.

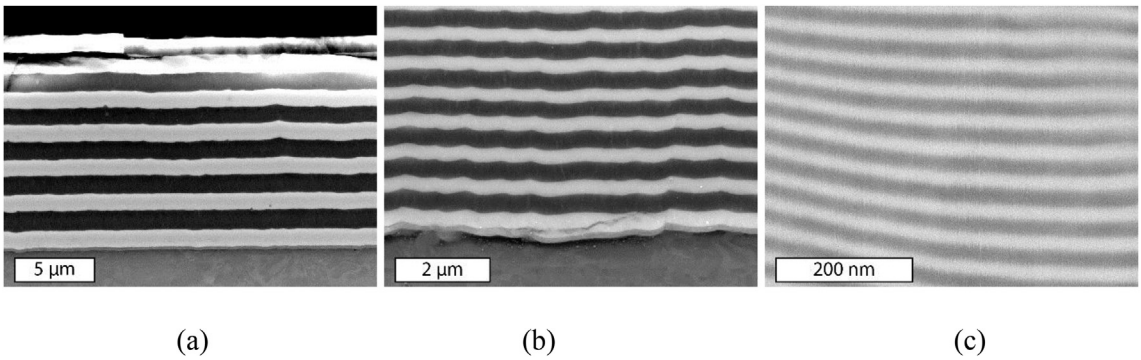

Fig. 3. SEM-images of polished cross-section samples 1 (a), 3 (b) and 6 (c) of multilayer CrN/MoN coatings.

Table 2
Total thickness and thickness of layer period measured by SEM on cross-sections.

Sample	Dep. time per layer, s	Bilayer thickness Λ, μm	Total thick., μm	Dep. rate, nm/s
1	300	2.26	13.5	3.8
2	150	1.18	14.7	3.9
3	80	0.60	13.6	3.8
4	40	0.25	11.1	3.2
5	20	0.12	10.8	2.9
6	10	0.044	7.8	2.2

4.2. Elemental composition

The analysis of elemental composition (see results in Table 3) was performed by WDS technique, which uses characteristic X-rays of interaction volume of studied films with electron beam. The process of data acquisition and analysis for elemental content and structures of considered films has the features described below.

The elemental composition of coatings was measured by scanning the presence of four of the most possible elements, assuming the contribution of chromium, molybdenum, nitrogen and oxygen.

The $K\alpha_1$ line of oxygen, which was used for the analysis ($E_{K\alpha1}(O) = 0.525$ keV), lies very close to the $L\alpha_1$ line of chromium ($E_{L\alpha1}(Cr) = 0.572$ keV). Because of this, chromium may contribute to the value of oxygen content in the film's composition. To avoid this, the determining of background for oxygen peak acquisition was made by shoulder on the side opposite to the chromium $L\alpha_1$ line.

Sample 1 demonstrates the presence of only Cr and N, which indicates that only the first top surface layer of CrN was exposed to interaction with the electron beam. It means that the thickness of the layers in sample 1 is much higher than the penetration depth of the electron beam used. Based on equation (1), it is possible to evaluate how deep into the film the electron beam goes. The electron beam used in this experiment may reach the depth of up to 0.34 or 0.54 μm for MoN or CrN films respectively. For coatings with thin enough layers, the average value of penetration depth was used. See the schematic illustration in Fig. 5.

In result, it was identified that in sample 1 with $\Lambda = 2.26$ μm, only the first layer of CrN was evaluated. The elemental composition was almost 50% both of chromium and nitrogen, ratio Cr/N = 1, which means that stoichiometric CrN film was deposited. The elemental composition of MoN in deposited samples was evaluated on the top layer of sample 2: Mo/N = 1.33. Also, assuming the same elemental ratios as for CrN in sample 1 and MoN in sample 2, it was estimated that integral elemental composition of sample 6 is as follows: Cr - 24.3 at.%, Mo - 26.8 at.%, N - 45.5 at.% and O - 3.4 at.%, which also gives the ratio Mo/Cr = 1.1. When compared with the measured values in Table 3 for sample 6 (with the thinnest layers, where the electron beam exposed about 22 layers), they are found to be similar, but slight decreasing of Mo fraction and (or) increasing of Cr content (ratio Mo/Cr = 0.9) are observed. Due to the unbalance of interaction volumes of CrN and MoN layers in samples 3, 4 and 5 (see Fig. 5), the results of performed WDS elemental analysis for mentioned films couldn't be considered as completely reliable.

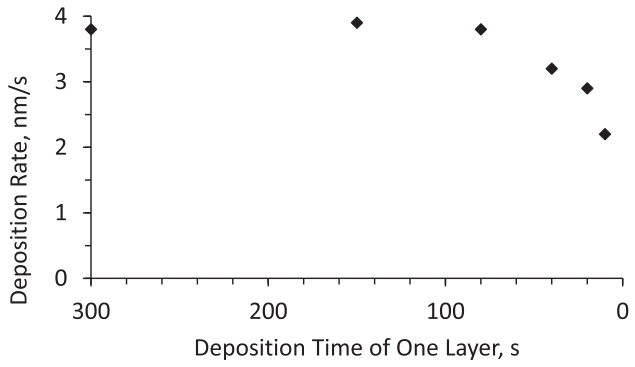

Fig. 4. Dependence of deposition rate on layer deposition time.

4.3. Morphology and microstructure

The surface morphology of CrN/MoN coatings with different

Table 3
Elemental concentration in CrN/MoN multilayer films taken by WDS.

Sample	Elements, WDS, top surface			
	Cr, at.%	Mo, at.%	N, at.%	O, at.%
1	48.1	0.1	50.1	1.8
2	1.1	53.0	41.0	5.0
3	1.8	50.3	43.1	4.8
4	10.2	41.6	43.5	4.7
5	25.5	16.0	56.7	1.8
6	27.6	25.1	44.8	2.5

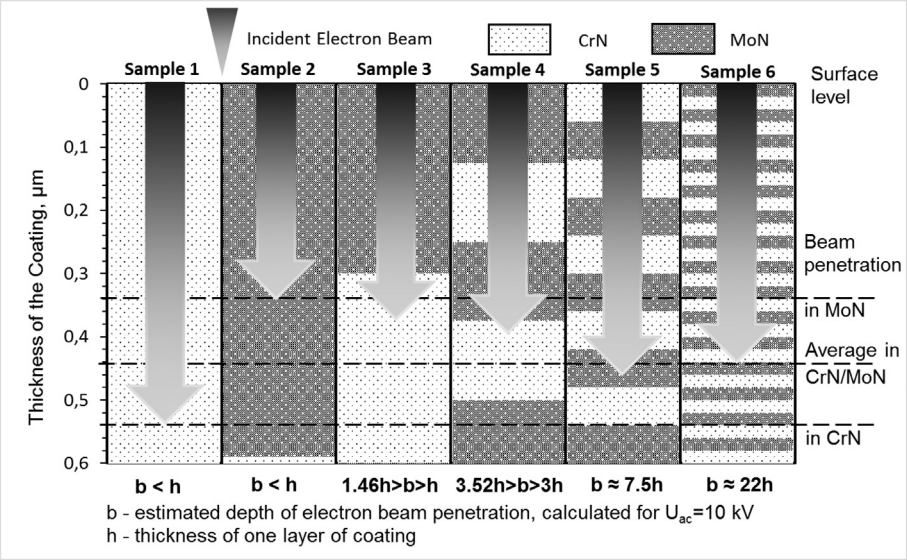

Fig. 5. Estimated penetration depth of electron beam (accelerated voltage U_{ac} = 10 kV) into multilayer CrN/MoN coatings with various bilayer thickness.

period thickness is presented in Fig. 6. From cross-section study and WDS analysis, it is proved that in Fig. 6(a) the thick top layer of sample 1 corresponds to CrN. The morphology is typical for chromium nitrides and it is characterised by high structuring, rocky and rough surface. The surface of sample 3 in Fig. 6(b) has contribution almost only from MoN layer and more flat surface was observed. Sample 6 shown in Fig. 6(c) with the thinner layers includes combined morphology of CrN and MoN films deposited by Arc-PVD.

Fig. 7 shows the set of XRD patterns recorded on all samples in θ/2θ geometry. Four main reflections, in the range of 35–82° are observed. The XRD lines positions of reference powders, including cubic phases γ-Mo_2N and CrN, tetragonal β-Mo_2N and hexagonal β-Cr_2N, are reported on the top bar. Some of them are characterised by similar crystal structure and (or) close peak positions, which leads to the overlapping and broadening of the experimental resulting peaks, which renders the phase determination not evident. However, the XRD patterns show that CrN/MoN coatings are polycrystalline.

To distinguish between the different possible phases, additional GIXRD and in-plane diffraction analysis were performed on the thickest samples, sample 1 (top layer – CrN) and sample 2 (top layer – MoN), for which only the top layer of the coating will contribute to the XRD signal under this configuration.

Fig. 8(a) shows the comparison of GIXRD pattern, in-plane pattern and conventional θ/2θ scans for sample 1. Clear reflections from cubic CrN phase are observed. Comparing the in-plane and conventional θ/2θ XRD patterns, one can infer from the change in Bragg peak positions that the top CrN layer is under compressive stress.

Fig. 8(b) shows the comparison of in-plane diffraction patterns (ω = 0.6°) for samples 1 (top layer is CrN) and 2 (top layer is MoN). They clearly demonstrate similar positions of peaks, which explains the overlapping of XRD lines on the integral pattern (Fig. 7) and confirm the presence of cubic (NaCl type) high temperature phase of γ-Mo_2N and CrN. The diffraction peaks inherent to β-Mo_2N or β-Cr_2N were not detected.

Summarising all the diffraction data mentioned above, the presence of two main phases in multilayer coatings can be inferred in Fig. 8: γ-Mo_2N and CrN with cubic (structural type NaCl) crystal lattices. They don't show any preferential crystal orientation: crystallites with [111], [100] and [311] orientations are detected, with a minor contribution from [220] ones. With decreasing bilayer period, the peaks get broadened, which could be related to reduction of crystallite size in these polycrystalline samples. The results of crystallite size calculation are presented in Table 4.

The average crystallite size was calculated using Scherrer equation (2). To extract information about separate peaks and to know the full width at half maximum (FWHM) the fittings of the XRD peaks were performed using the Crystal Impact's phase

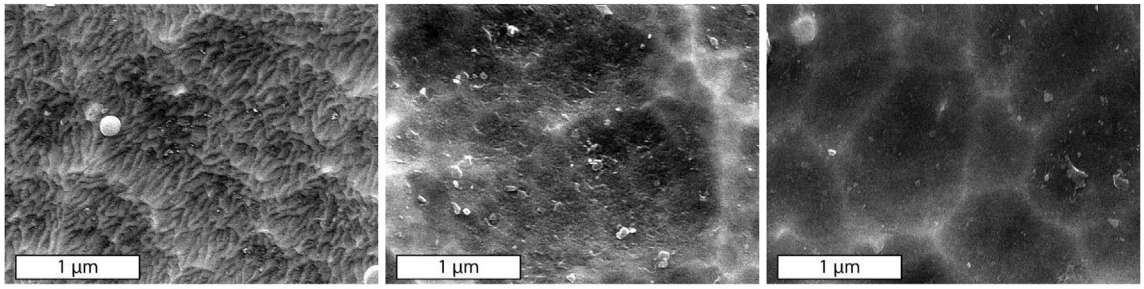

Fig. 6. SEM-images of multilayer CrN/MoN coatings surface for samples 1 (a), 3 (b) and 6 (c).

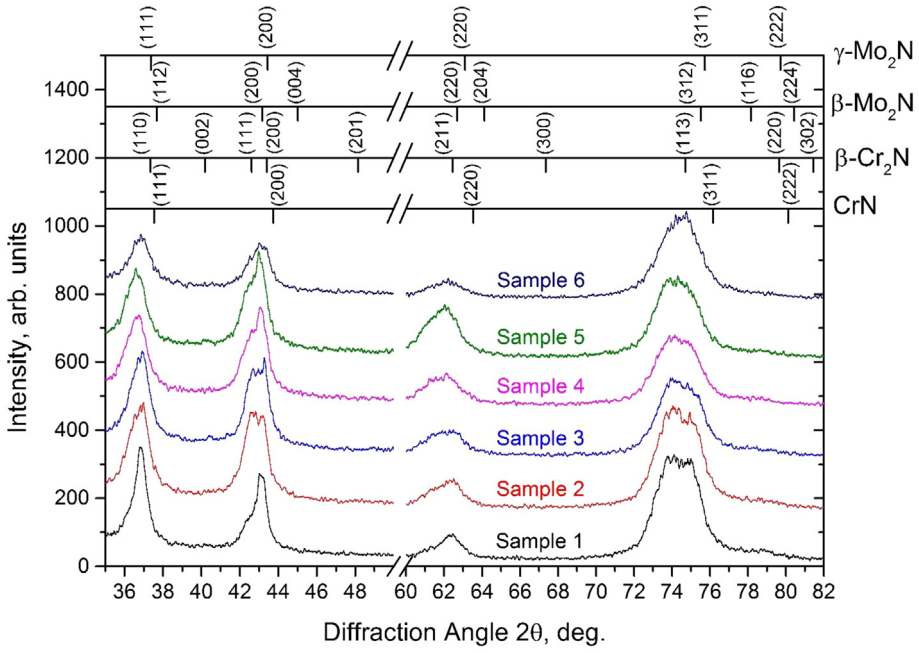

Fig. 7. XRD patterns for CrN/MoN multilayer coatings in the range 2θ from 35 to 82° with specified possible phases and planes orientation indicated on the top bar. The range of 50–60° has been cut due to the absence of diffraction peaks and for a better view of the patterns.

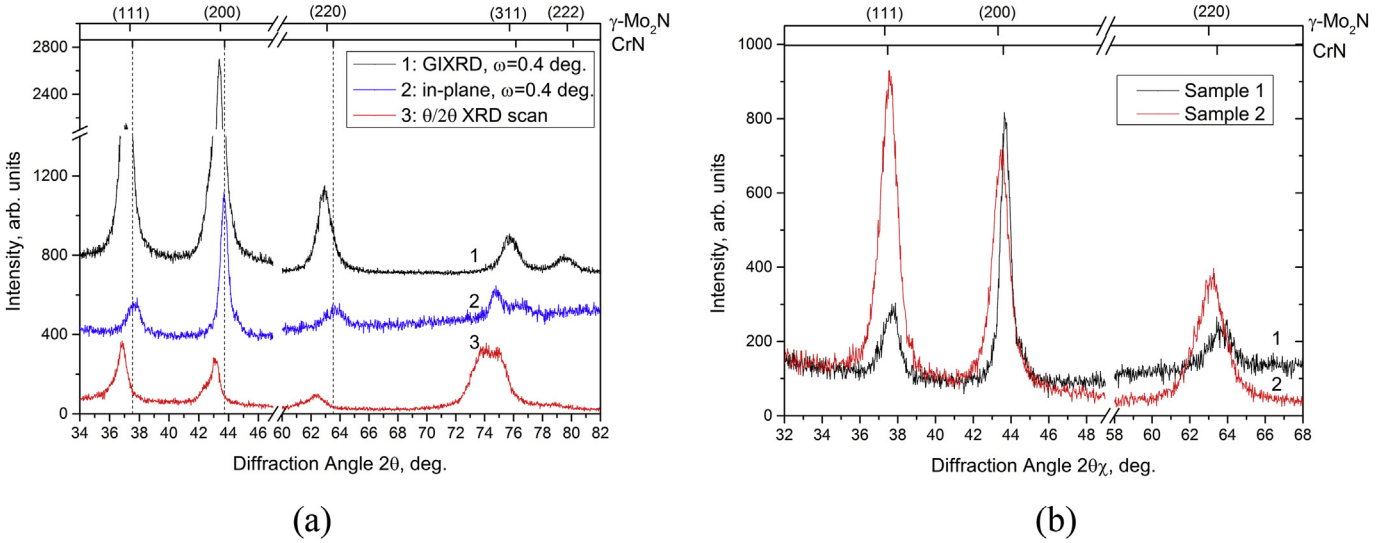

Fig. 8. Experimental X-ray diffraction patterns: (a) - sample 1 taken in asymmetrical grazing incidence mode (1), in-plane (2) and symmetrical θ/2θ scans (3); (b) – samples 1 and 2, in-plane mode, ω = 0.6°. Cut ranges of diffraction angle don't contain any diffraction peaks.

identification software "Match!". Any other factors which can contribute to the width of a diffraction peak besides crystallite size, such as instrumental effects, microstrain, solid solution inhomogeneity etc. have not been taken into account. With the reduction of layer thickness in studied CrN/MoN multilayer films the crystallite size also decreases.

Additional information on the crystal orientation, grain size, and their dependence on the layer thickness was gained from EBSD analysis (see Fig. 9). Note that the colours used in Fig. 9(a) don't denote any crystal orientation, and grains are simply coloured to distinguish them from neighbouring grains. Fig. 9(a) shows an example of a unique grain colour map for part of the CrN layer for sample 1. Reconstructed ellipse shaped grains demonstrate columnar structure and films growth. To supplement the information about the films structure, the inverse pole figure map was used. The inverse pole figure map is a colour coded map, where the colour gives an indication of the crystal direction aligned with sample normal. Fig. 9(b) demonstrates exactly the same part of the coating as Fig. 9(a), but in inverse pole figure mode, and it is seen that some small mis-orientation is present in grains. Neighbour grains may have similar crystal orientations or completely different ones.

The EBSD analysis shows the columnar growth of the deposited multilayer CrN/MoN films, as well as the prevailing texture formation. Fig. 10 presents one of the pole figures for sample 1 with the highest fibre texture in the orientation (311). These

Table 4
Calculation of crystallite and grain size for multilayer CrN/MoN coatings.

Sample number	Crystallite size for selected phase and lattices orientation, nm								Average grain size by EBSD, μm
	CrN				γ-Mo_2N				
	(111)	(200)	(311)	(220)	(111)	(200)	(311)	(220)	
1	17.2	14.3	8.9	–	6.4	11.5	8.1	–	0.16
2	14.0	13.9	8.7	–	5.6	10.4	8.0	–	0.15
3	14.5	13.5	8.4	–	5.6	9.9	8.0	–	0.14
4	14.2	12.1	8.2	–	7.4	9.3	7.4	–	0.11
5	13.7	9.9	7.7	–	9.4	9.0	7.2	–	–
6	9.3	8.3	7.6	–	5.8	8.0	7.0	–	–
1 (in-plane)	7.7	14.7	9.7	5.5	–	–	–	–	–
2 (in-plane)	–	–	–	–	10.4	9.0	6.5	6.3	–

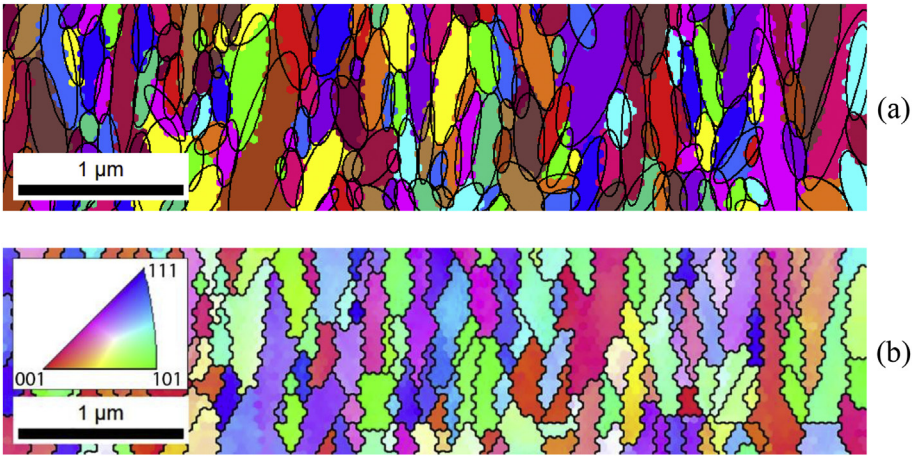

Fig. 9. EBSD mapping for CrN layer of sample 1: unique grain colour map with shape ellipses boundaries (a), inverse pole figure [311] (b). (For interpretation of the references to colour in this figure legend, the reader is referred to the web version of this article.)

results are also in agreement with the XRD patterns analysis, where the high intensity of (311) texture was detected for sample 1 (see Figs. 7 and 8).

The discussed method also allows evaluation of a grain size in coatings and to build graphs of their distribution. From Fig. 11, it is clear that coatings with smaller layer thickness have smaller grain size. It is seen that sample 4 (with the lowest layer thickness of all four analysed) has the lowest fraction of the largest grains, as well as higher values for the smallest grains size. The opposite is observed for sample 1 with the thicker layers. Samples 2 and 3 demonstrate gradient transition between the two described states. The detailed information about grain size for studied samples is shown in the last column of Table 4. The statistics were taken from the same cross-section areas sizes with height of the total films thickness and width of 5.3 μm. It should also be noted that the Y-axis is presented in arbitrary units of fraction, which are not absolute values, to avoid some deviations due to possible small differences in size or range of studied zone of cross-section samples.

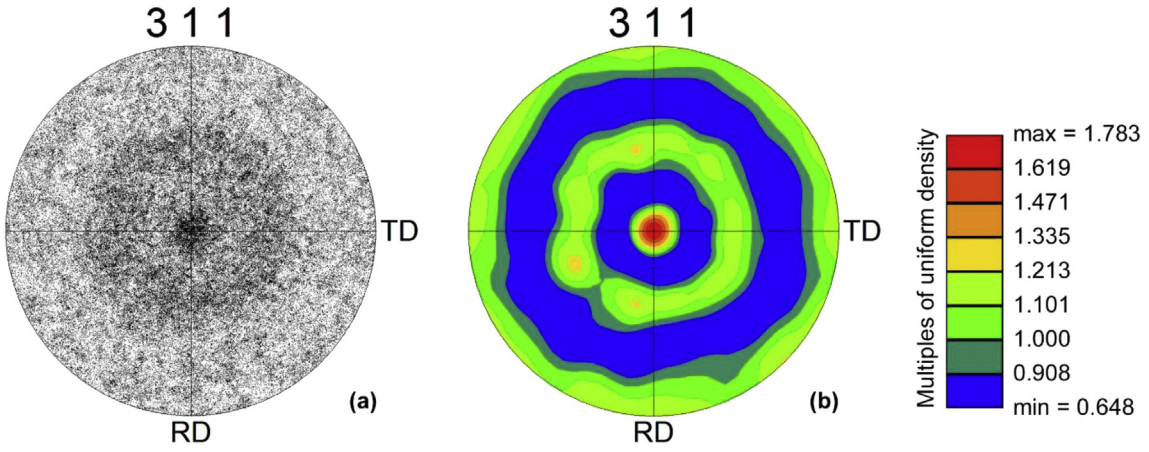

Fig. 10. One of the pole figures and texture calculations for sample 1.

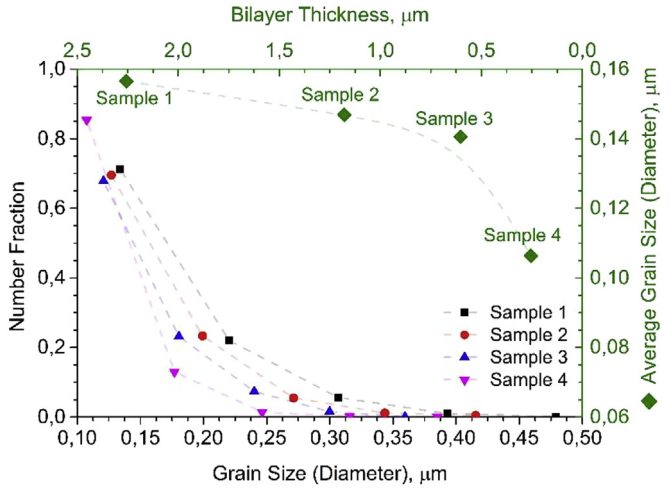

Fig. 11. Grain size distribution and average grain size values in CrN/MoN multilayer coatings with different bilayer thickness.

4.4. Evaluation of residual stresses

The residual stress was determined on samples 1 and 2, giving access to the stress state of the topmost layers, MoN and CrN, respectively. For each sample, several hkl reflections were recorded using asymmetric XRD 2θ scans and the stress was derived using the $\sin^2\psi$ method. As seen from Fig. 12, both layers are under compressive stress, as manifested from the negative slopes of $\sin^2\psi$ plots. Detailed results of stress and lattice parameters evaluation are reported in Table 5. For both CrN and γ-Mo_2N phases the in-plane $a_{\parallel}$ (resp. out-of-plane $a_{\perp}$) lattice parameters are lower (resp. larger) than reference values from the literature, which is consistent with the existence of biaxial compressive stress. The stress-free lattice parameter, a_0, was calculated from equation (3) [48]:

$$a_0 = a_{\perp}\left(\frac{1-\nu}{1+\nu}\right) + a_{\parallel}\left(\frac{2\nu}{1+\nu}\right), \quad (3)$$

where ν is the Poisson ratio, taken 0.29 both for CrN and MoN [42,51,52]. Larger compressive stress was found for the MoN layer compared to CrN one (see Table 5), which may be due to higher incorporation of nitrogen atoms in the crystal lattice and correlates with the results of elemental composition analysis. For the same reason the increasing of stress-free lattice parameters a_0 in comparison to reference values a_{ref} is observed.

The stress and strain calculated for MoN layer have relatively higher values in comparison to CrN; further, calculated lattice parameter a_0 is significantly higher than that of reference γ-Mo_2N, which could be also explained by the presence of the cubic, off-stoichiometric MoN_x metastable phase. This metastable cubic MoN_x phase has a higher lattice constant than γ-Mo_2N, as a result of filling of unoccupied nitrogen sites [54]. As already reported by Linker et al. [55] and Perry et al. [56], this increase of the lattice parameter (0.419–0.427 nm) happens with increasing nitrogen contents (MoN_x, $0.9 < x < 1.3$). Nitrogen atoms in excess may occupy the 50% vacant octahedral sites of γ-Mo_2N phase and additionally they can also occupy interstitial sites, resulting in lattice expansion [57]. This conclusion is also supported by the N content (and oxygen content), which may together justify the presence of that phase [58].

4.5. Mechanical properties

Results of measurements of mechanical properties are presented in Fig. 13. Values of hardness and elastic modulus (see Fig. 13(a)) are shown, vis-a-vis values of bilayer thickness in samples. It was observed that with decrease in bilayer thickness, the hardness and Young's Modulus increase. The lowest values of hardness and Young's Modulus, typical for pure chromium nitrides, correspond to the film with the thicker layers (H = 25 GPa, E = 295 GPa when Λ = 2.26 μm) and the highest – for the films with the thinner layers (H = 38 GPa, E = 357 GPa when Λ = 44 nm). It should be noted that values of measured hardness higher than 40 GPa were observed in some zones of three samples 4, 5 and 6 with the lowest values of bilayer thickness – up to 42.3 GPa, so the deposited films may belong to group of superhard coatings.

To evaluate mechanical properties of films and to predict protective features of coatings, the ratios of hardness to elastic modulus could be used. In the past decade, it was shown that values of ratios H/E and H^3/E^2 are very important parameters [10,59,60].

The ratio H/E (or H/E*, where $E^* = E/(1 - \nu^2)$) plays a significant role in the so-called "plasticity index", widely recognised as a reliable parameter of elastic behaviour of surface in contact with external forces. It could characterise protective properties of coatings in terms of cracking, abrasive wear and serve as a ranking parameter for toughness of the deposited films.

In Fig. 13(b) the area can be divided into two zones by line H/E = 0.1. Three samples are placed in zone with higher ratio of H/E > 0.1 (plastic area), which characterise them as coatings with enhanced wear resistance. Fig. 13(b, left Y-axis) demonstrates the

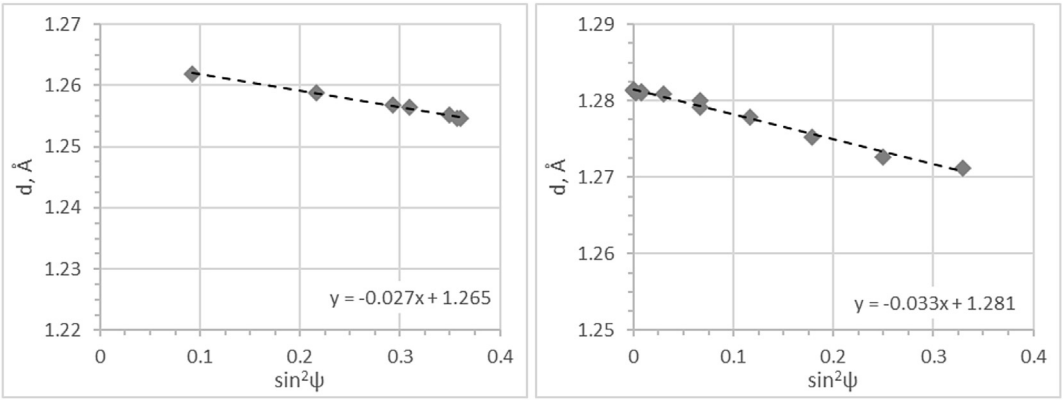

Fig. 12. $Sin^2\psi$ plots recorded for 311 reflections of CrN (a) and γ-Mo_2N (b) layers.

Table 5
Results of residual stresses calculation for multilayer CrN/MoN thin films.

Phase	Residual Stress σ, GPa							Lattice parameters, Å				ε, %
	Plane orientations						Average	$a_{\perp}$	$a_{\parallel}$	a_0	a_{ref} [53]	
	111	200	220	311	222	400						
CrN	7.1	4.6	5.7	5.0	6.3	3.1	5.3	4.196	4.134	4.168	4.149	1.5
γ-Mo_2N	8.8	4.6	8.2	5.8	–	–	6.9	4.248	4.153	4.205	4.163	2.3

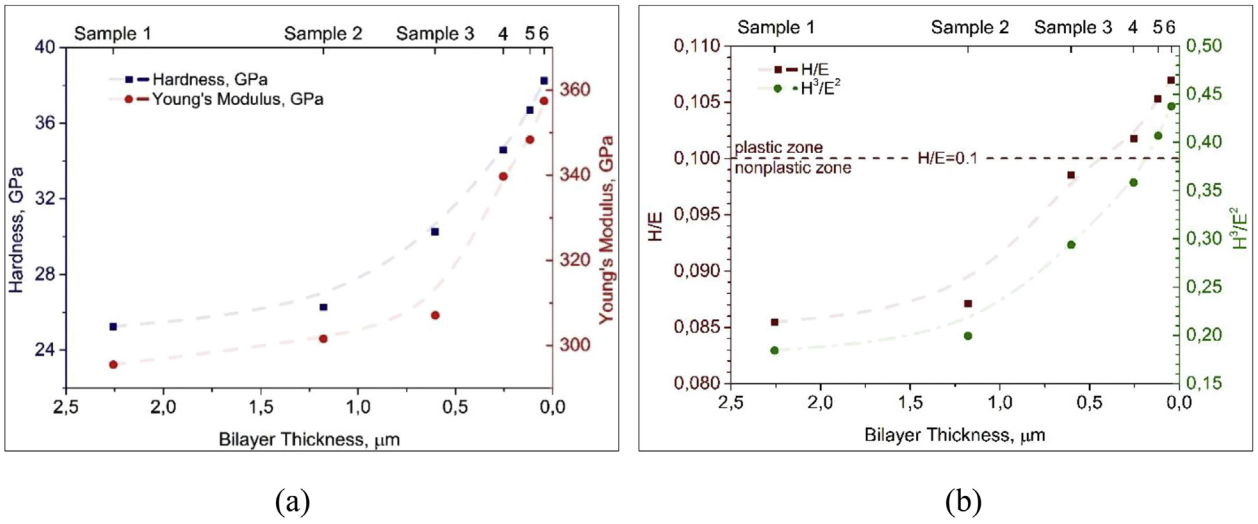

(a) (b)

Fig. 13. Results of mechanical tests: hardness and Young's modulus measurements (a), dependence of H/E and H^3/E^2 ratios on the bilayer thickness of CrN/MoN films (b).

dependence of ratio H/E on bilayer thickness. The thinner the layers in coating, the higher was the ratio H/E achieved.

The ratio H^3/E^2 is another important parameter of mechanical properties characterisation, which allows determination and rank coatings in relation to plastic deformation resistance. The behaviour of ratio H^3/E^2 in terms of films bilayer thickness is described in Fig. 13(b, right Y-axis). The observed improvement of the mechanical parameters, such as hardness and following H/E or H^3/E^2 ratios in studied multilayer films, may most likely be related to the decrease of bilayer thickness and subsequently lower values of crystalline/grain sizes. This leads to an increase in interface volume and role of boundaries as pinning points in material. The Hall-Petch strengthening with decrease of layer thickness leads to prevention of dislocation movements and will enhance yield strength of material and increase the hardness.

As the bilayer thickness becomes thinner, a higher number of layers were produced. It leads also to the increasing of interlayer interfaces, which block the propagation of cracks and dislocations, avoid the continuity of pinholes and pores [61]. Recent work by Daniel et al. [62] on the beneficial impact of interface design on crack deflections have been reported in TiN coatings.

5. Conclusions

The multilayer coatings of CrN and MoN films deposited by Arc-PVD have been studied. The focus of study was on the methods of elemental composition and structural characterisation, mechanical properties and their comparison. It was observed that CrN/MoN coatings deposited by Arc-PVD are characterised by a relatively sharp interface between layers; they have typical columnar structure growth, and prevailing crystal orientations with textures (111), (200) and (311) of cubic γ-Mo_2N and CrN phases. When most of the deposition conditions are maintained fixed and only the deposition time per sample is changing, the coatings keep stable similar phases and elemental composition (at least in range of the bilayer thickness considered in the present paper), but the structure is changing through decreasing of grains size in coatings with lower values of layer thickness. On one hand, it leads to the increase of the interfaces volume in CrN/MoN coatings. On the other hand, the number of interlayer interfaces increases due to the decrease of individual layer thickness. The mentioned changes lead to Hall-Petch strengthening of films, and to the blocking of cracks and dislocations propagation in multilayer CrN/MoN coatings. The measured hardness has reached values of 42.3 GPa.

It is an important property of the studied material, which may cause future enhancement of mechanical properties and result in application of multilayer films as super-hard protective coatings. Future studies will focus on the thermal stability, oxidation and chemical resistance to expand the range of possible applications. The observed properties and obtained results show potential of their use for physical and mechanical property control and prediction in coatings and thin films.

Acknowledgements

The study was partly financed by the Foundation of Science and Technology (FCT) of Portugal, project UID/NAN/50024/2013, budget project of Ministry of Education and Science of Ukraine “Physical basics of forming the composition and properties of transition metals boride, nitride and boride-nitride films for application in machine-building” (number 0116U002621) and Erasmus Mundus scholarship from European Commission (grant number 2013-2526/001-001). B.O. Postolnyi is also grateful to Arlete Apolinário from LEPABE, Department of Chemical Engineering, Faculty of

Engineering of the University of Porto, and to João H. Belo from IFIMUP and IN - Institute of Nanoscience and Nanotechnology, Physics and Astronomy Department, Faculty of Sciences of the University of Porto, for help and useful discussion.

References

[1] A.D. Pogrebnjak, A.A. Bagdasaryan, I.V. Yakushchenko, V.M. Beresnev, The structure and properties of high-entropy alloys and nitride coatings based on them, Russ. Chem. Rev. 83 (2014) 1027–1061.

[2] A.D. Pogrebnyak, M.K. Kylyshkanov, Y.N. Tyurin, A.S. Kaverina, I.V. Yakushchenko, A.A. Borisenko, B.A. Postol'ny, I.A. Kulik, Properties and structure of oxidized coatings deposited onto Al-Cu and Al-Mg alloys, Technol. Phys. 57 (2012) 840–848.

[3] S. Veprek, Recent search for new superhard materials: go nano!, J. Vac. Sci. Technol. A Vac. Surf. Film. 31 (2013) 50822.

[4] P.H. Mayrhofer, C. Mitterer, L. Hultman, H. Clemens, Microstructural design of hard coatings, Prog. Mater. Sci. 51 (2006) 1032–1114.

[5] J. Musil, Hard nanocomposite coatings: thermal stability, oxidation resistance and toughness, Surf. Coat. Technol. 207 (2012) 50–65.

[6] A. Cavaleiro, J.T.M. De Hosson (Eds.), Nanostructured Coatings, Springer New York, New York, NY, 2006.

[7] S. Veprek, M.G.J. Veprek-Heijman, P. Karvankova, J. Prochazka, Different approaches to superhard coatings and nanocomposites, Thin Solid Films 476 (2005) 1–29.

[8] P.C. Wo, X.L. Zhao, P.R. Munroe, Z.F. Zhou, K.Y. Li, D. Habibi, Z.H. Xie, Extremely hard, damage-tolerant ceramic coatings with functionally graded, periodically varying architecture, Acta Mater. 61 (2013) 193–204.

[9] A.D. Pogrebnjak, V.M. Rogoz, O.V. Bondar, N.K. Erdybaeva, S.V. Plotnikov, Structure and physicomechanical properties of NbN-based protective nanocomposite coatings: a review, Prot. Met. Phys. Chem. Surf. 52 (2016) 802–813.

[10] V. Ivashchenko, S. Veprek, A. Pogrebnjak, B. Postolnyi, First-principles quantum molecular dynamics study of $Ti_xZr_{1-x}N(111)/SiN_y$ heterostructures and comparison with experimental results, Sci. Technol. Adv. Mater. 15 (2014) 25007.

[11] T. Polcar, A. Cavaleiro, High-temperature tribological properties of CrAlN, CrAlSiN and AlCrSiN coatings, Surf. Coat. Technol. 206 (2011) 1244–1251.

[12] M.K. Samani, X.Z. Ding, N. Khosravian, B. Amin-Ahmadi, Y. Yi, G. Chen, E.C. Neyts, A. Bogaerts, B.K. Tay, Thermal conductivity of titanium nitride/titanium aluminum nitride multilayer coatings deposited by lateral rotating cathode arc, Thin Solid Films 578 (2015) 133–138.

[13] G. Abadias, P. Djemia, L. Belliard, Alloying effects on the structure and elastic properties of hard coatings based on ternary transition metal (M=Ti, Zr or Ta) nitrides, Surf. Coat. Technol. 257 (2014) 129–137.

[14] F. Wang, D. Holec, M. Odén, F. Mücklich, I.A. Abrikosov, F. Tasnádi, Systematic ab initio investigation of the elastic modulus in quaternary transition metal nitride alloys and their coherent multilayers, Acta Mater. 127 (2017) 124–132.

[15] N. Ghafoor, I. Petrov, D.O. Klenov, B. Freitag, J. Jensen, J.E. Greene, L. Hultman, M. Odén, Self-organized anisotropic $(Zr_{1-x}Si_x)N_y$ nanocomposites grown by reactive sputter deposition, Acta Mater. 82 (2015) 179–189.

[16] M.I. Yousaf, V.O. Pelenovich, B. Yang, C.S. Liu, D.J. Fu, Effect of bilayer period on structural and mechanical properties of nanocomposite TiAlN/MoN multilayer films synthesized by cathodic arc ion-plating, Surf. Coat. Technol. 282 (2015) 94–102.

[17] K. Yalamanchili, I.C. Schramm, E. Jiménez-Piqué, L. Rogström, F. Mücklich, M. Odén, N. Ghafoor, Tuning hardness and fracture resistance of ZrN/$Zr_{0.63}Al_{0.37}N$ nanoscale multilayers by stress-induced transformation toughening, Acta Mater. 89 (2015) 22–31.

[18] G. Abadias, V.V. Uglov, I.A. Saladukhin, S.V. Zlotski, G. Tolmachova, S.N. Dub, A.J. van Vuuren, Growth, structural and mechanical properties of magnetron-sputtered ZrN/SiN_x nanolaminated coatings, Surf. Coat. Technol. 308 (2016) 158–167.

[19] J. Lackner, L. Major, M. Kot, Microscale interpretation of tribological phenomena in Ti/TiN soft-hard multilayer coatings on soft austenite steel substrates, Bull. Pol. Acad. Sci. Tech. Sci. 59 (2011) 343–355.

[20] F. Vaz, J. Ferreira, E. Ribeiro, L. Rebouta, S. Lanceros-Méndez, J.A. Mendes, E. Alves, P. Goudeau, J.P. Rivière, F. Ribeiro, I. Moutinho, K. Pischow, J. de Rijk, Influence of nitrogen content on the structural, mechanical and electrical properties of TiN thin films, Surf. Coat. Technol. 191 (2005) 317–323.

[21] P. Mayrhofer, F. Kunc, J. Musil, C. Mitterer, A comparative study on reactive and non-reactive unbalanced magnetron sputter deposition of TiN coatings, Thin Solid Films 415 (2002) 151–159.

[22] Z.H. Xie, M. Hoffman, P. Munroe, R. Singh, A. Bendavid, P.J. Martin, Microstructural response of TiN monolithic and multilayer coatings during microscratch testing, J. Mater. Res. 22 (2007) 2312–2318.

[23] L.A. Rocha, E. Ariza, J. Ferreira, F. Vaz, E. Ribeiro, L. Rebouta, E. Alves, A.R. Ramos, P. Goudeau, J.P. Rivière, Structural and corrosion behaviour of stoichiometric and substoichiometric TiN thin films, Surf. Coat. Technol. 180–181 (2004) 158–163.

[24] A. Gilewicz, B. Warcholinski, Tribological properties of CrCN/CrN multilayer coatings, Tribol. Int. 80 (2014) 34–40.

[25] T. Polcar, R. Martinez, T. Vítů, L. Kopecký, R. Rodriguez, A. Cavaleiro, High temperature tribology of CrN and multilayered Cr/CrN coatings, Surf. Coat. Technol. 203 (2009) 3254–3259.

[26] Y.X. Ou, J. Lin, S. Tong, W.D. Sproul, M.K. Lei, Structure, adhesion and corrosion behavior of CrN/TiN superlattice coatings deposited by the combined deep oscillation magnetron sputtering and pulsed dc magnetron sputtering, Surf. Coat. Technol. 293 (2016) 21–27.

[27] Z.X. Yang, X.Y. Kuang, Z.H. Wang, M.M. Zhong, X.F. Huang, The mechanical properties of MoN under high pressure and effect of metallic bonding on its hardness, Solid State Sci. 28 (2014) 20–25.

[28] H. Hazar, Characterization of MoN coatings for pistons in a diesel engine, Mater. Des. 31 (2010) 624–627.

[29] M. Nordin, M. Larsson, S. Hogmark, Mechanical and tribological properties of multilayered PVD TiN/CrN, TiN/MoN, TiN/NbN and TiN/TaN coatings on cemented carbide, Surf. Coat. Technol. 106 (1998) 234–241.

[30] A.K. Kuleshov, V.V. Uglov, V.V. Chayevski, V.M. Anishchik, Properties of coatings based on Cr, Ti, and Mo nitrides with embedded metals deposited on cutting tools, J. Frict. Wear 32 (2011) 192–198.

[31] I. Jauberteau, A. Bessaudou, R. Mayet, J. Cornette, J. Jauberteau, P. Carles, T. Merle-Méjean, Molybdenum nitride films: crystal structures, synthesis, mechanical, electrical and some other properties, Coatings 5 (2015) 656–687.

[32] V.P. Anitha, S. Major, D. Chandrashekharam, M. Bhatnagar, Deposition of molybdenum nitride thin films by r.f. reactive magnetron sputtering, Surf. Coat. Technol. 79 (1996) 50–54.

[33] O.V. Bondar, B.A. Postol'nyi, V.M. Beresnev, G. Abadias, P. Chartier, O.V. Sobol, D.A. Kolesnikov, F.F. Komarov, M.O. Lisovenko, A.A. Andreev, Composition, structure and tribotechnical properties of TiN, MoN single-layer and TiN/MoN multilayer coatings, J. Superhard Mater. 37 (2015) 27–38.

[34] B.O. Postolnyi, P. Konarski, F.F. Komarov, O.V. Sobol', O.V. Kyrychenko, D.S. Shevchuk, Study of elemental and structural phase composition of multilayer nanostructured TiN/MoN coatings, their physical and mechanical properties, J. Nano- Electron. Phys. 6 (2014) 4016.

[35] A.D. Pogrebnjak, V.M. Beresnev, O.V. Bondar, G. Abadias, P. Chartier, B.A. Postol'nyi, A.A. Andreev, O.V. Sobol', The effect of nanolayer thickness on the structure and properties of multilayer TiN/MoN coatings, Tech. Phys. Lett. 40 (2014) 215–218.

[36] V.M. Beresnev, O.V. Bondar, B.O. Postolnyi, M.O. Lisovenko, G. Abadias, P. Chartier, D.A. Kolesnikov, V.N. Borisyuk, B.A. Mukushev, B.R. Zhollybekov, A.A. Andreev, Comparison of tribological characteristics of nanostructured TiN, MoN, and TiN/MoN arc-PVD coatings, J. Frict. Wear 35 (2014) 374–382.

[37] A.D. Pogrebnjak, G. Abadias, O.V. Bondar, B.O. Postolnyi, M.O. Lisovenko, O.V. Kyrychenko, A.A. Andreev, V.M. Beresnev, D.A. Kolesnikov, M. Opielak, Structure and properties of multilayer nanostructured coatings TiN/MoN depending on deposition conditions, Acta Phys. Pol. A 125 (2014) 1280–1283.

[38] A.D. Pogrebnjak, D. Eyidi, G. Abadias, O.V. Bondar, V.M. Beresnev, O.V. Sobol, Structure and properties of arc evaporated nanoscale TiN/MoN multilayered systems, Int. J. Refract. Met. Hard Mater. 48 (2015) 222–228.

[39] R.A. Koshy, M.E. Graham, L.D. Marks, Synthesis and characterization of CrN/Mo_2N multilayers and phases of Molybdenum nitride, Surf. Coat. Technol. 202 (2007) 1123–1128.

[40] S.S. Grankin, V.M. Beresnev, O.V. Sobol, V.A. Stolbovoy, V.Y. Novikov, S.V. Lytovchenko, U.S. Nyemchenko, A.A. Meylehov, M.G. Kovaleva, A.A. Postelnik, I.N. Toryanik, Structure, substructure, hardness and adhesion strength of multiperiod composite coatings MoN/CrN, J. Nano- Electron. Phys. 7 (2015), 4050–1-4050–5.

[41] V.M. Beresnev, S.A. Klimenko, O.V. Sobol', S.S. Grankin, V.A. Stolbovoi, P.V. Turbin, V.Y. Novikov, A.A. Meilekhov, S.V. Litovchenko, L.V. Malikova, Effect of the deposition parameters on the phase–structure state, hardness, and tribological characteristics of Mo_2N/CrN vacuum–arc multilayer coatings, J. Superhard Mater. 38 (2016) 114–122.

[42] B. Bouaouina, A. Besnard, S.E. Abaidia, F. Haid, Residual stress, mechanical and microstructure properties of multilayer Mo_2N/CrN coating produced by R.F Magnetron discharge, Appl. Surf. Sci. 395 (2017) 117–121.

[43] B. Postolnyi, O. Bondar, M. Opielak, P. Rogalski, J.P. Araújo, Structural analysis of multilayer metal nitride films CrN/MoN using electron backscatter diffraction (EBSD), in: M. Vladescu, R. Tamas, I. Cristea (Eds.), Proc. SPIE - Int. Soc. Opt. Eng., 2016, p. 100100E.

[44] B.O. Postolnyi, J.P. Araujo, Structural analysis of Arc-PVD multilayer metal nitride coatings CrN/MoN using electron backscatter diffraction (EBSD), in: 2016 Int. Conf. Nanomater. Appl. Prop., IEEE, 2016, 01NTF16-1-01NTF16-4.

[45] B. Postolnyi, J.P. Araújo, A. Pogrebnjak, Applying of electron backscatter diffraction (EBSD) for studying structural and phase composition of multilayer CrN/MoN coatings fabricated by Arc-PVD, in: Eur. Microsc. Congr. 2016 Proc., Wiley-VCH Verlag GmbH & Co. KGaA, Weinheim, Germany, 2016, pp. 673–674.

[46] P.J. Potts, Electron probe microanalysis, in: A Handb. Silic. Rock Anal., Springer US, Boston, MA, 1987, pp. 326–382.

[47] P. Scherrer, Bestimmung der Größe und der inneren Struktur von Kolloidteilchen mittels Röntgenstrahlen, Nachrichten von Der Gesellschaft Der Wissenschaften Zu Göttingen, Math. Kl. 1918 (1918) 98–100.

[48] D. Gall, C.-S. Shin, T. Spila, M. Odén, M.J.H. Senna, J.E. Greene, I. Petrov, Growth of single-crystal CrN on MgO(001): effects of low-energy ion-irradiation on surface morphological evolution and physical properties, J. Appl. Phys. 91 (2002) 3589–3597.

[49] S. Wroński, K. Wierzbanowski, A. Baczmański, A. Lodini, C. Braham, W. Seiler, X-ray grazing incidence technique—corrections in residual stress

measurement—a review, Powder Diffr. 24 (2009) S11–S15.
[50] M.E. Fitzpatrick, A.T. Fry, P. Holdway, F.A. Kandil, J. Shackleton, L. Suominen, Determination of residual stresses by X-ray diffraction - issue 2, in: Meas. Good Pract. Guid. No. 52, National Physical Laboratory, Teddington, UK, 2005.
[51] C. Sarioglu, U. Demirler, M.K. Kazmanli, M. Urgen, Measurement of residual stresses by X-ray diffraction techniques in MoN and Mo_2N coatings deposited by arc PVD on high-speed steel substrate, Surf. Coat. Technol. 190 (2005) 238–243.
[52] U. Wiklund, M. Bromark, M. Larsson, P. Hedenqvist, S. Hogmark, Cracking resistance of thin hard coatings estimated by four-point bending, Surf. Coat. Technol. 91 (1997) 57–63.
[53] Powder Diffraction Files: card 065-2899 for fcc-CrN, card 025-1366 for fcc-γ-Mo2N.
[54] F.F. Klimashin, N. Koutná, H. Euchner, D. Holec, P.H. Mayrhofer, The impact of nitrogen content and vacancies on structure and mechanical properties of Mo–N thin films, J. Appl. Phys. 120 (2016) 185301.
[55] G. Linker, R. Smithey, O. Meyer, Superconductivity in MoN films with NaCl structure, J. Phys. F. Met. Phys. 14 (1984) L115–L119.
[56] A.J. Perry, A.W. Baouchi, J.H. Petersen, S.D. Pozder, Crystal structure of molybdenum nitride films made by reactive cathodic arc evaporation, Surf. Coat. Technol. 54–55 (1992) 261–265.
[57] J. Lowther, Lattice model for the properties of non-stoichiometric cubic and hexagonal molybdenum nitride, J. Alloys Compd. 364 (2004) 13–16.
[58] J. Barbosa, L. Cunha, L. Rebouta, C. Moura, F. Vaz, S. Carvalho, E. Alves, E. Le Bourhis, P. Goudeau, J.P. Rivière, Properties of MoN_xO_y thin films as a function of the N/O ratio, Thin Solid Films 494 (2006) 201–206.
[59] D.M. Marulanda, J.J. Olaya, U. Piratoba, A. Mariño, E. Camps, The effect of bilayer period and degree of unbalancing on magnetron sputtered Cr/CrN nano-multilayer wear and corrosion, Thin Solid Films 519 (2011) 1886–1893.
[60] A. Leyland, A. Matthews, On the significance of the H/E ratio in wear control: a nanocomposite coating approach to optimised tribological behaviour, Wear 246 (2000) 1–11.
[61] T.Y. Tsui, G.M. Pharr, W.C. Oliver, C.S. Bhatia, R.L. White, S. Anders, A. Anders, I.G. Brown, Nanoindentation and nanoscratching of hard carbon coatings for magnetic disks, MRS Proc. 383 (1995) 447–452.
[62] R. Daniel, M. Meindlhumer, W. Baumegger, J. Zalesak, B. Sartory, M. Burghammer, C. Mitterer, J. Keckes, Grain boundary design of thin films: using tilted brittle interfaces for multiple crack deflection toughening, Acta Mater. 122 (2017) 130–137.